Photochemistry and Photobiology, 2017, 93: 558–568

The Properties and Activity of TiO_2/beta-SiC Nanocomposites in Organic Dyes Photodegradation

Katarzyna Pstrowska*[1], Bartłomiej Maciej Szyja[1], Hanna Czapor-Irzabek[2], Adam Kiersnowski[3] and Jerzy Walendziewski[1]

[1]Division of Fuels Chemistry and Technology, Faculty of Chemistry, Wrocław University of Science and Technology, Wrocław, Poland
[2]Laboratory of Elemental Analysis and Structural Research, Faculty of Pharmacy, Wrocław Medical University, Wrocław, Poland
[3]Polymer Engineering & Technology Division, Faculty of Chemistry, Wroclaw University of Science and Technology, Wrocław, Poland

Received 19 September 2016, accepted 13 November 2016, DOI: 10.1111/php.12705

ABSTRACT

The TiO_2/beta-SiC nanocomposites containing 0–25 wt. % of beta-SiC were synthesized by the sol-gel method and tested in the photodegradation of methylene blue and methyl orange water solutions. With the increase in SiC content, only a slight decrease in energy band gap was observed (3.19–3.12 eV), together with significant increase in the surface area of the catalysts (42.7–80.4 $m^2\ g^{-1}$). In the synthesized material, the anatase phase of TiO_2 was present in the form of small agglomerates resulting from the mechanical mixing process. In the process conditions (catalyst concentration 0.5 $g\ L^{-1}$, initial dye concentration 100 ppm, light source 100 W UV-Vis lamp), we have observed no signs of catalyst deactivation. The significantly higher photodegradation activity of methylene blue than methyl orange can be attributed to the preferable pH of the solution compared to pH_{PZC} and the cationic character of the first dye. In case of methyl orange, pH process conditions substantially limit the contact of the catalyst with the dye, as negatively charged surface of the catalysts repels the dissociated anionic dye molecules.

INTRODUCTION

The key step in the process of drinking water purification and wastewater treatment is the degradation of the organic pollutants, which is a complex and multistep process by its nature. The semiconductor-based photocatalysts play here one of the most important roles, due to their ability to form the electron/hole pairs upon the irradiation with UV or visible light. The charge carriers—electron in the conductance band (CB) and the hole in the valence band (VB) generated this way—participate in the redox reactions (1).

The amount of literature devoted to this subject is extensive. The exact mechanism of these reactions depends on the particular semiconductor and particular organic compound undergoing decomposition, with two main pathways emerging (2). The photooxidation mechanism is indirect and proceeds via the formation of hydroxyl radicals out of water or surface hydroxyl groups that in turn oxidize the organic molecule in the solution. Interestingly, this reaction can occur without the direct contact of the organic molecule with the surface of the catalyst. The other option occurs via direct oxidation of the pollutant by the positively charged hole from the VB of the semiconductor. The latter mechanism implies the necessity of the adsorption of the pollutant on the surface of the photocatalyst. In addition, this mechanism requires that the VB of the semiconductor has higher oxidation potential than the molecule oxidized. Contrary to this, the relatively small oxidation potential of 1.23 V is needed for indirect oxidation by hydroxyl radicals. More detailed information can be found in the review paper of Zangeneh (3).

A particular place in the photocatalysis field is taken by TiO_2 and TiO_2-containing systems, which are widely studied due to the properties of this material: high efficiency, low cost, physical and chemical stability in typical reaction conditions, abundance and noncorrosive properties (4). Despite these advantages, several improvements are still needed before the industrial use of TiO_2 becomes possible. The main disadvantage is the inability to utilize wide solar spectrum in efficient and cost-effective catalysis due to the relatively large band gap amounting to 3.2 eV for anatase and 3.0 eV for rutile (5,6).

One way to improve the photocatalytic performance of TiO_2 is the deposition of metal or nonmetal particles on TiO_2 surface or the substitution of the framework atoms in the structure of TiO_2 with heteroatoms (7–9). These heteroatoms create additional electronic states in the band structure of the catalyst that allow to trap the electrons/holes and prevent their fast recombination. Another approach is to alter the properties of the material, such as its stability and activity by means of coupling the TiO_2 with other materials in the procedure known as band engineering. This often leads to the synergistic photocatalytic effect of semiconductors coupling (10,11), which is caused by the improved charge transfer mechanism in the heterojunctions. This effect has been confirmed for many different photoactive processes—from the improved photocurrent generation (12) to the catalytic water splitting (13).

In the field of the photodegradation of pollutants, Ge *et al.* (14) reported efficient decomposition of methylene orange (MO)

*Corresponding author email: katarzyna.pstrowska@pwr.edu.pl (Katarzyna Pstrowska)

on a TiO_2 anatase and ZnO wurtzite composite. The reaction mechanism proposed there was the indirect oxidation by hydroxyl radicals. However, no comparison to the pure TiO_2 system nor the role of the ZnO was discussed. Li *et al.* (15) reported a $BiFeO_3/TiO_2$ nanocomposite active in the visible light range. The authors reported efficient photodegradation of Congo red and attributed it to the enhanced rate of charge separation.

An interesting material for the formation of the nanocomposites with the TiO_2 is 3C-SiC, also known as β-SiC. It has a cubic structure and exhibits excellent physical and chemical properties essential in heterogeneous catalytic reactions. Most important of them are as follows: high thermal conductivity, low specific weight, insolubility in water and chemical inertness and the lowest band gap energy (2.36 eV) among other commonly used hexagonal SiC structures: 4H-SiC (3.20 eV) and 6H-SIC (3.00 eV) (8). Recent paper of Digdaya *et al.* (16) describes in detail the coupling of the a-SiC photocathodes with an amorphous TiO_2 coatings in a form of the hetero p–i–n junction, to enhance the photoactivity in the water splitting process. Using Mott–Schottky analysis, authors estimated the conduction band edge position and the electronic properties of the (n) TiO_2 and verified the electron transfer mechanism through the conduction band.

Lai and Tsai suggested the reduced charge recombination in a β-SiC–TiO_2 system used as a photoelectrode in a dye-sensitized solar cell (DSSC) is responsible for enhanced power conversion with these materials (17). Compared with a pristine nanocrystalline TiO_2, a DSSC based on a 3C-SiC (0.04 wt%)/TiO_2 nanocomposite photoelectrode was reported an increase in power conversion efficiency by 115%.

The literature concerning the photodegradation of organic pollutants by the SiC–TiO_2 nanocomposites is limited. The coupling of SiC and TiO_2 semiconductors was presented by Hao *et al.* (18). Authors conclude that SiC is characterized by the more negative conduction band than that of TiO_2 and upon excitation by UV light the electrons are transferred from SiC to TiO_2. It was suggested that such phenomenon limits the electrons recombination process, what in turn positively influences the photocatalysis efficiency.

Similarly, the photogenerated charge separation was confirmed as the main factor leading to the enhanced photocatalytic activity in the photodegradation of Rhodamine B (100 ppm solution), indigo carmine (20 ppm solution) and methylene blue (20 ppm solution) (19,20). These findings are also in line with the different nanocomposite β-SiC—Ag_3PO_4/Ag/SiC. This catalyst was also reported as responsible for effective photodegradation of diluted methyl orange and phenol (both at the initial concentration of 10 ppm) solutions (21). Importantly, in all these cases, the catalyst concentration was relatively high (1 g L^{-1}). In our view, the excess of the catalyst is the main reason for the substantial catalytic activity reported in these studies for diluted dye solutions (concentration as low as 10–20 ppm). The main focus of these investigations was maximizing the efficiency of the catalysts, and as such, the goal has been achieved and the pollutants underwent quick photodegradation. This effect can be even more pronounced for catalysts obtained by the sol-gel method, characterized by relatively large surface area. Although the adsorption of the organic compounds is not considered to be the prerequisite for the photodegradation in the mechanism of indirect oxidation by hydroxyl radicals, it is suggested to improve the reaction kinetics (4,22,23). This maximum efficiency approach, however, brings little insight into the understanding of the mechanism, and for this reason, in this work we extend the analysis to the less efficient approach, where the kinetics of the reaction can be evaluated.

Another important factor which is a point of the interest of this study is the pH of the solution. This factor is often disregarded, and so far, little consensus has been achieved in the interpretation of semiconductors coupling. Doong *et al.* reported that in alkali conditions, the charge of the surface of the TiO_2 catalyst becomes negative, what favors direct aromatic ring cleavage (24). On the contrary, the low pH induces changes in protonation of the surface, which can shift the Fermi level of the semiconductor, so that a photocatalyst can become a better oxidant in low pH (25). This effect is discussed in details in the manuscript.

In the present work, photocatalytic tests have been carried out with the catalyst concentration of 0.5 g L^{-1} and 100 ppm of methylene blue (MB) and methyl orange (MO) each. To estimate the influence of SiC on the photocatalytic activity of the anatase, the catalysts containing 0–25 wt.% of SiC have been synthesized by TiO_2 deposition on β-SiC by simple sol-gel method. We present detailed analysis of the influence of β-SiC content on the crystal structure, morphology, optical and adsorptive properties of the catalyst, as well as its surface state (pH_{PZC}) on the photocatalytic activity of the β-SiC–TiO_2 nanocomposites.

MATERIALS AND METHODS

Synthesis of TiO_2/β-SiC nanocomposites. A series of TiO_2/β-SiC heterojunction composites were synthesized by sol-gel method, similar to the method described by Mishra *et al.* (19) and Gómez-Solis *et al.* (20). The method involved the hydrolysis of titanium (IV) isopropoxide (TIP —$C_{12}H_{28}O_4Ti$—97%, Aldrich) in the presence of β-SiC (200-450 mesh, Aldrich) in concentration varying from 5 to 25 wt.%. The β-SiC was dispersed in 30 mL of dry ethanol at room temperature and subsequently sonificated for 15 min. SiC dispersed in ethanol was further heated up to the temperature of 70°C, and TIP was added slowly (1–2 drops min^{-1}) to achieve the desired amount of TiO_2 in the ethanol–SiC solution. During this process, the system was kept in agitation at constant temperature of 70 ± 1°C. To promote hydrolysis–condensation process, immediately after TIP addition, certain amount of a mixture of water/acetic acid (55 wt. % ratio, $nH_2O/nC_{12}H_{28}O_4Ti$ = 4:1) was added. At this stage, the reaction mixture was kept in agitation for 1 h. The formed gel was dried in 80°C for 5 h. Finally, dry powder was milled and thermally treated at 450°C for 3 h (heating rate of 2°C min^{-1}). The respective catalysts obtained with the specified content of SiC are listed in Table 1.

Material characterization. The structure and phase of the prepared samples were identified by the X-ray powder diffraction (XRD). The measurements were carried out using the Rigaku Ultima IV X-ray diffractometer fitted with 2 kW X-ray tube operated at 40 kV and 30 mA (CuKα, λ = 0.1542 nm), slit collimation system, Nickel CuKβ

Table 1. The composition of the TiO_2/β-SiC catalysts prepared by the sol-gel method.

	β-SiC	TiO_2
Catalyst designation	wt. %	
SiC-0	0	100
SiC-5	5	95
SiC-10	10	90
SiC-15	15	85
SiC-20	20	80
SiC-25	25	75
SiC-100	100	0

filter and a scintillation counter. The instrument was working in Bragg–Brentano, symmetric step-scan mode (θ-θ). The average instrumental broadening for the above conditions determined from measurements of SiC and Si crystals was found to be approx. 0.05°(2θ). In the measurements, 200–250 mg crystalline (coarse powder) samples were placed on glass holders and scanned in the range from 20° to 90.0° in 0.005° steps with exposure of 0.5 s per each point. For the quantitative analysis, the data were processed (smoothed, corrected for background and $K\alpha_2$, etc.) in Integral Analysis for Windows ver. 6.0 software (Rigaku Inc.) and, further in OriginPro 8.6 for Windows. Analysis of the individual peaks and the resulting crystalline phases were performed by the Miller assignments according to Refs. (26,27).

UV–Vis diffuse reflectance spectra were recorded with the use of UV–Vis–NIR Cary 5 equipped with an adapter for diffuse reflection spectra recording. Powder samples were placed in the sample holder and scanned in the range of 190–900 nm. As a standard for testing, barium sulfate was used. The measurements were performed three times to eliminate an eventual error. The observed differences in spectral deviations did not exceed 1–2%. Band gap energy values were calculated directly from the diffuse reflectance measurements (graphical method). The optical band gap (E_g) was determined from the equation: $E_g = 1239.84/v$, where v is the intersection of the tangent with the x-axis (28,29).

To determine the textural properties of the obtained catalysts, the nitrogen adsorption at 77 K was measured using Quantachrome Autosorb 1-C. Before the analysis, all samples were outgassed at 423 K for 4 h under high vacuum (3.75×10^{-3} Torr). The specific surface area (S_{BET}) was calculated by the Brunauer–Emmett–Teller (BET) method. Total pore volume (V_{TOT}) was derived from the amount of nitrogen vapor adsorbed at a relative pressure close to unity, by assumption that the pores were then filled with liquid adsorbate. Average pore diameter (ADP) was obtained from total pore volume and BET surface area assuming cylindrical pore geometry.

The pH at which the catalyst surface charge takes a zero value (pH_{PZC}) was determined according to the method described by Moreno-Castilla *et al.* (30). Catalyst size measurements were performed using dynamic light scattering (DLS) using Malvern Zetasizer Nano-ZS ZEN3600 (Malvern Instruments, Malvern, UK). Samples were irradiated with red light (HeNe laser, wavelength $\lambda = 633$ nm), and the intensity fluctuations of the scattered light (detected at a backscattering angle of 173°) analyzed to obtain an autocorrelation function. All samples were dispersed in water (with the catalyst concentration at the level of 0.001 wt. %) and sonificated for 5 and 15 min. The tested samples (1 mL) were measured in disposable polystyrene cuvettes at the temperature of 25°C, and this temperature was actively maintained within 0.1°C in the sample chamber. Before each analysis, samples were equilibrated for 25 s at 25°C. The following assumptions were made in the analysis: The viscosity of the solution was assumed to be same as of water, corrected for temperature ($\eta = 0.888$ mPa.s); the solution refractive index was that of water ($n = 1.33$); the refractive index of the particle was selected to be nR = 2.60 with an absorption of nI = 0.01. Data were acquired in the automatic mode.

Pictures of the photocatalysts surface were taken with Scanning Electron Microscope (SEM)—Jeol JSM-6610LVnx. Distribution of individual elements in the catalyst mass was determined with Energy Dispersive Spectrometer (EDS)—Oxford Aztec Energy. Before the test, samples were coated with carbon. For that reason, the exact calculation of each element content was not possible in this study.

Photocatalytic degradation. Photodegradation was performed using the closed system with inner-irradiation-type quartz reactor, illustrated in Fig. 1. A medium pressure mercury lamp (Ace Glass Co., power of 100 W) was used as the light source. The lamp was immersed in a quartz well with cooling medium. Coolant temperature was kept at the level of 10°C with the use of flow cryostat (Julabo FP-50) to prevent any thermal degradation of the model compounds used. Each experiment was performed according to the following procedure: 400 mL of the dye solution (100 ppm concentration) was put in the reactor with the 0.2 g of the catalyst (catalyst concentration at the level of 0.5 g L^{-1}). The suspension was cooled and mixed in dark with the magnetic stirrer for 60 min. After 1 h of the adsorption process, first sample of the solution was taken from the reactor (zero time), the dye concentration was estimated and marked as initial dye concentration for the photodegradation process (C_0). After the adsorption process, UV lamp was turned on. The efficiency of the photocatalysts was verified based on the samples taken every 15 min until the total time of 5 h of the lamp operation. After catalyst separation, the dye concentration in the taken sample was estimated with Hitachi U-2001 Spectrophotometer, at 664 nm and 463 nm for methylene blue (MB) and methyl orange (MO) respectively. Basing on the results, the photocatalytic degradation efficiency of cationic MB and anionic MO dyes was calculated by the following equation:

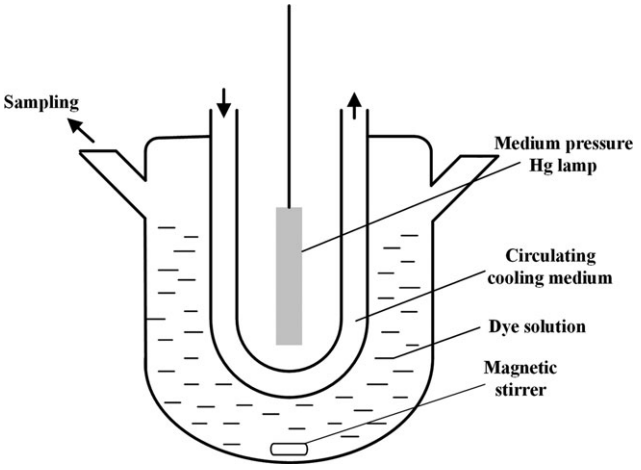

Figure 1. Experimental setup for photocatalytic degradation.

$$\text{Photodegradation efficiency}\,(\%) = \frac{C_0 - C_t}{C_0} \times 100\%$$

where C_0 and C_t denote dye concentration at time of exposure zero and t, respectively.

The photocatalytic degradation of diluted MB and MO solutions is a pseudo-first-order reaction and its kinetics may be expressed as $\ln(C_0/C) = kt$, where k is the apparent rate constant, C_0 and C are the dye concentrations at zero time of exposure (after 1 h of adsorption process) and after irradiation for t hour, respectively. For each catalyst, the photodegradation process was performed twice for confirmation. Variations of the results did not exceed 3%.

Computational procedure. The simulations have been carried out using the TURBOMOLE version 6.6 (31). The dye molecules have been used in their ionic form, that is anion of the MO and cation of MB. The geometries of the models have been optimized using the DFT method. The PBE0 (32) and Def2-TZVP basis set (33,34) have been used in the optimization. The ADC(2) method (35) and cc-pVDZ basis set (36–38) has been employed to calculate the excited states of the dyes. The vertical excitation spectrum has been calculated for 6 singlet and 3 triplet states for each dye molecule. The geometries in the S1 and T1 states have been optimized with the same ADC(2) method. The conical intersection has been optimized using the procedure of Szabla *et al.* (39).

RESULTS AND DISCUSSION

Characterization of the photocatalysts

Diffraction patterns shown in Fig. 2 suggest that only anatase phase of TiO_2 is present in all catalysts regardless of the SiC and TiO_2 content (SiC-5–SiC-25). For reasons of clarity in reading the individual peaks, the XRD patterns of only SiC-15, SiC-0 and SiC-100 are presented. The average crystalline domain size of 14 nm has been calculated by putting the widths at half maxima measured for A101 reflection (diffraction angle at the level of 25 2θ/°) for SiC-0 catalyst into Scherrer's formula in the way as described in Ref. (40). The sol-gel method of TiO_2 deposition on the surface of SiC does not alter neither phase purity nor sizes of crystalline domains. The diffraction pattern of the example SiC-15 material reveals only reflections characteristic of the

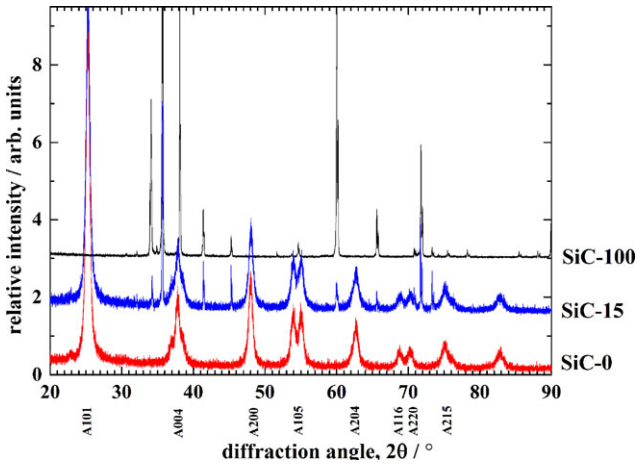

Figure 2. Raw powder diffraction patterns (with $K\alpha_2$ intensities included) recorded for SiC-0, SiC-15 and SiC-100. The patterns are shifted along the intensity scale for clarity. Assignment of Miller indices was based on literature (26,27).

anatase phase and peaks from SiC having integral intensities roughly proportional to its content (cf. the pattern of the SiC-100, Fig. 2). The average sizes of crystalline domains, as calculated from the width of A101 peak, were found to be 14 nm, identical as in sample SiC-0. In all remaining SiC–TiO_2 samples (SiC-5–SiC-25), the average crystalline sizes of anatase measured in the direction normal to the (A101) planes were also found to be approximately 14 nm.

Figure 3 shows the optical response of SiC-0, SiC-10 and SiC-20 catalysts. The other results are omitted for clarity. The calculation results for all analyzed catalysts are summarized in Table 2. The results indicate that the heterojunction of TiO_2 and SiC only slightly decreases the energy band gap (Eg) value. Intuitively, one could expect that the bigger content of SiC in the catalyst, the smaller observed Eg, because Eg value of SiC-100 is the smallest among investigated materials (2.29 eV—Table 2). On the contrary, increased amount of SiC in the TiO_2/β-SiC catalysts does not significantly decrease band gap energy. More pronounced is the shift in the absorbance of the light toward the visible region (Fig. 3). As expected, the maximum shift of the

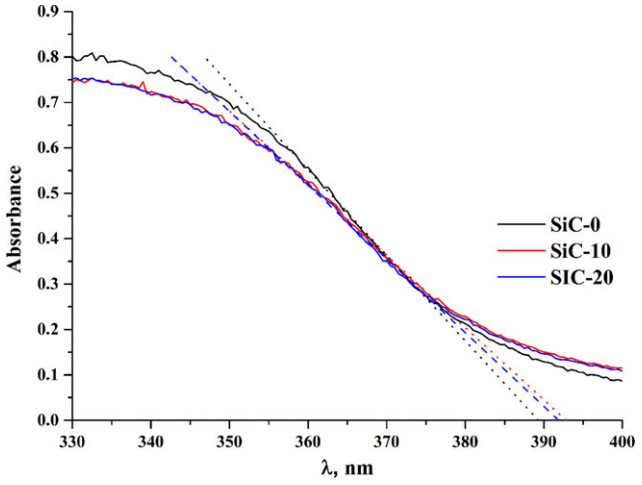

Figure 3. UV–Vis–DR results for the graphical Eg determination.

Table 2. Textural, surface and optical properties of the synthesized catalysts.

Catalyst	S_{BET}, $m^2\ g^{-1}$	ADP, nm	V_{TOT}, $cm^3\ g^{-1}$	pH_{PZC}	Band gap energy, eV
SiC-0	42.7	10.4	0.153	5.85	3.19
SiC-5	45.5	11.6	0.148	5.67	3.13
SiC-10	48.6	14.9	0.170	5.61	3.16
SiC-15	50.7	12.0	0.152	5.53	3.16
SiC-20	60.1	13.1	0.142	5.54	3.16
SiC-25	80.4	14.5	0.189	5.76	3.12
SiC-100	17.1	16.2	0.001	7.62	2.29

wavelength toward the visible region was observed in case of SiC-25 (the point of intersection with the *x*-axis—397.3 nm). Even so, by comparing the intersection of the sample with 100 wt. % SiC (SiC-100) of 540.7 nm and with the pure anatase sample (SiC-0)—389.3 nm, it can be noticed that the observed shift is insignificant.

Slight changes in the energy band gap values may be the result of the chosen synthesis type. In the first stage of the synthesis, titanium precursor is dropwise added into a solution of ethanol, which contains SiC particles. The dispersion of the precursor in the ethanol solution is determined by the rate of the addition and the solution temperature. At the next step, the titanium precursor is hydrolyzed and deposited at the SiC particles present in the solution. This is one of two key steps that are responsible for the dispersion of TiO_2 on the SiC surface.

Critical analysis suggests that the sol-gel synthesis of TiO_2 on the selected silicon carbide particles could be improved. Relatively large and irregular shaped SiC particles (200-450 mesh, Aldrich—Fig. 4) tend to fall to the bottom of the glass of the reaction despite intensive stirring. This limits the contact of SiC surface with the hydrolyzed precursor of titanium.

After the step of hydrolysis and gelation, titanium is initially deposited on the surface of SiC. Gel drying is followed by the fragmentation and calcination of the material. This has an important impact on both the energy band gap and the efficiency of the charge separation during photoexcitation. As an example, the dispersion of TiO_2 on the SiC-15 catalyst is presented in Fig. 5. In our opinion, the use of particles of small size and relatively regular shapes could improve the titanium oxide dispersion on the SiC surface. As far as the catalyst surface is concerned, one might think that increasing the amount of SiC will improve the dispersion of titanium on its surface and consequently will increase the photocatalytic activity. It can be seen that the increased amount of SiC not only affects the BET surface of the catalysts (Table 2), but slightly alters the energy band gap value. This means that the silicon carbide creates sort of a platform and together with the active phase increases the chance of a contact with the solution. Therefore, it should favorably influence the course of the photocatalytic process. On the other hand, TiO_2 agglomerates are too large to effectively reduce the band gap energy of the entire catalyst.

Similar results demonstrating the increase in the surface area of the catalyst with increased content of SiC were presented by Mishra *et al.* (19), where SiC particles were obtained from the rice husk. The average pore diameter of the SiC particles was determined to be ~40 nm, and the surface area was slightly larger (20 $m^2\ g^{-1}$) than in case of the SiC used by us (ca. 17 $m^2\ g^{-1}$). The analysis of the surface structure suggests that

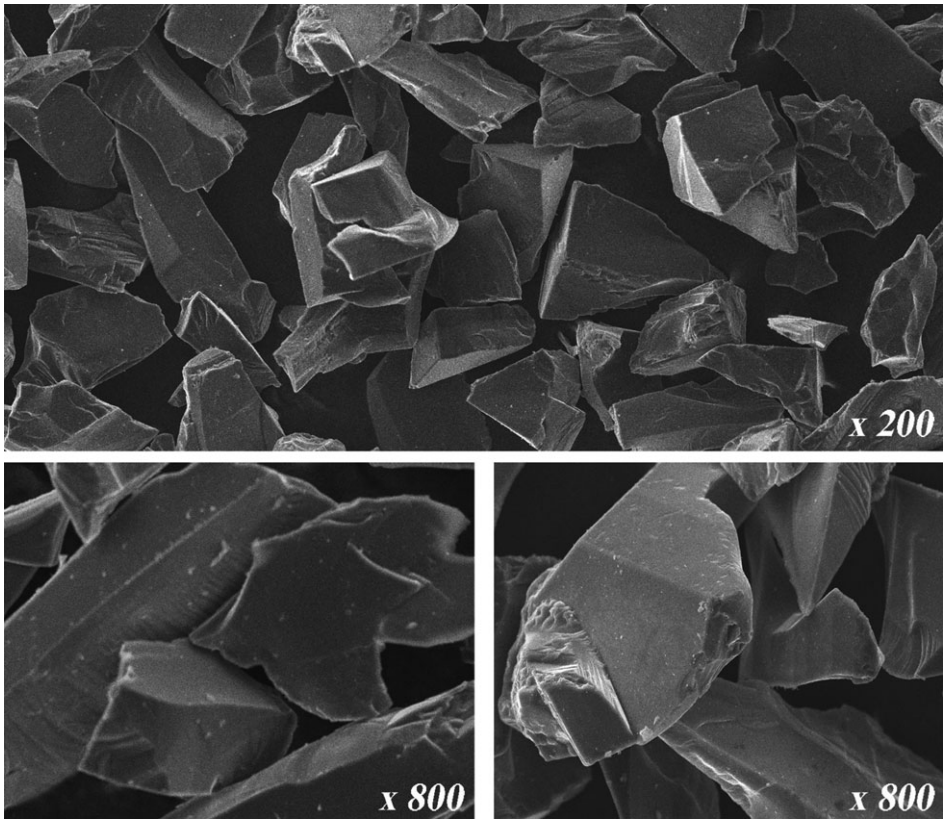

Figure 4. SEM pics of the SiC-100 surface shape.

the materials obtained by us in the sol-gel synthesis have similar characteristics. The increased surface area of the material, however, was not observed for the materials obtained by Gómez-Solis *et al.* (20).

Much bigger differences can be observed in case of the textural properties of the synthesized materials and respective pH_{PZC} values (Table 2). Anatase (SiC-0) is characterized by pH_{PZC} value of 5.85. Sol-gel sedimentation of titania on the SiC surface results in the decrease in the pH_{PZC} value to the range of 5.53–5.76. Under acidic or alkaline condition, the surface of titania can be protonated or deprotonated, respectively, according to the following reactions (41). This effect which will influence photocatalytic effectiveness depending on the solution properties:

$$\begin{aligned} &pH < pH_{PZC} \qquad TiOH + H^+ \rightarrow TiOH_2^+ \\ &pH > pH_{PZC} \qquad TiOH + OH^- \rightarrow TiO^- + H_2O \end{aligned}$$

Thus, the surface of each catalyst will be positively charged when in contact with the solution of pH below pH_{PZC} and negatively charged in the solution with pH value above pH_{PZC}. Change in charge of the catalyst is an important factor which can influence mainly the adsorption process (first, "dark" stage of the photocatalysis). Indirectly, it can also affect the process of photodegradation, where the contact of catalyst surface with the reactants increases the reaction rate (22,23). Thus, the pH of the reaction medium, which can affect the reactant repulsion from the surface of the catalyst or, conversely, increase the contact time, is an important factor. The organic compound type used for photodegradation is equally important and will be discussed in the Adsorption of the organic pollutants section.

Another factor influencing the contact between organic compound and the catalyst surface is the catalysts particle size and its mechanical resistance during the process. Several factors can influence the mechanical strength of the catalyst grain. They include the operating temperature, pH of the solution and the mixing time. In the present study, the temperature was kept at 25°C, which corresponds to the temperature of photodegradation process (20–30°C). The mixing was accomplished by means of the sonication initially for time of 5 min and subsequently for 15 min.

The distribution of particle size of the selected materials is presented in Fig. 6. With the increase in SiC content, broader range of the crystals size can be observed. It is clear that this is due to the large size of SiC particles. Interestingly, the size of TiO_2 agglomerates is influencing overall catalysts size distribution. This implies the favored formation of larger agglomerates of TiO_2 that are deposited on larger amount of SiC "platform." As it can be observed, the increase in sonication time (in case of real process of photodegradation with stirring time) results in deagglomeration of TiO_2. This phenomenon can improve the performance of the process, as deagglomeration can lead to the release of active TiO_2 particles into the reaction zone in time. It may therefore influence the otherwise linear course of degradation.

Adsorption of the organic pollutants

First stage of all photodegradation processes is the adsorption of the dye at the surface of the catalyst. Therefore, the increased

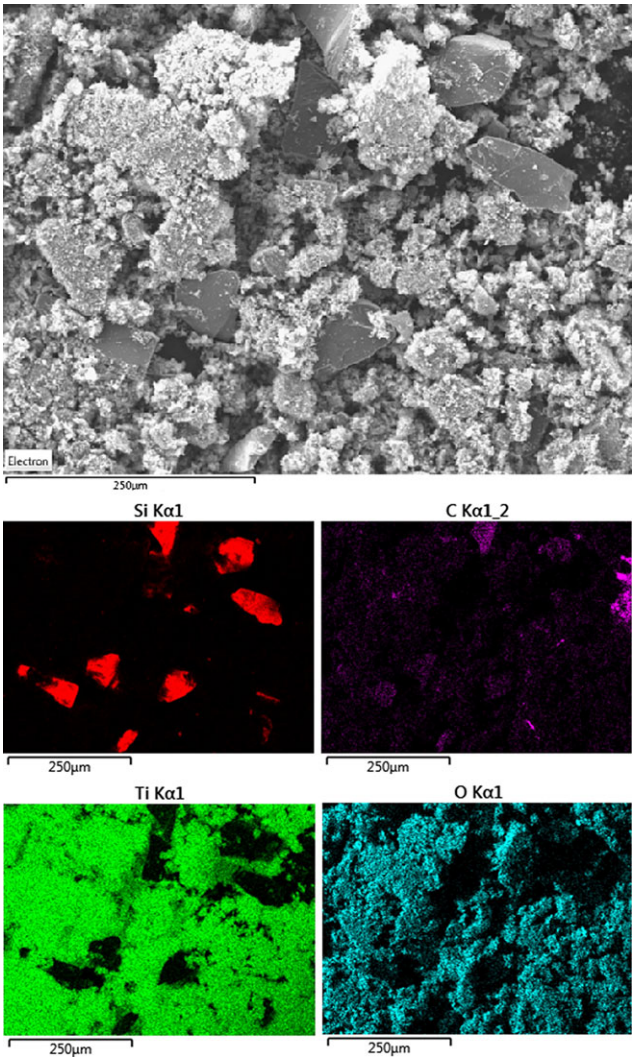

Figure 5. EDS elements mapping the surface of the SiC-15 catalyst.

surface area improves the adsorption processes, which in turn has a significant influence on the photodegradation. The adsorption of organic compounds from diluted aqueous solutions can be affected by the factors such as the molecular weight of the compound, size and geometrical shape of particles, functional groups, polarity, solubility and dissociation constant. Selected physicochemical properties of MB and MO are presented in Table 3.

The pH of MB and MO 100 ppm solutions was determined to be 7.21 and 6.55, respectively. In that case, both dyes were present in the solution in dissociated forms. The pH of the solution influences also the electric charge on the surface of the catalyst. In such case, dissociated form of the adsorbate interacts with the surface of the catalyst. Considering the pH of point of zero charge pH_{PZC} (Table 2), the surface of the SiC-0–SiC-25 catalysts is charged negatively. Only in case of pure β-SiC (SiC-100), whose pH_{PZC} equals to 7.62, positive charge on the surface of the catalyst can be expected. Negatively charged surface of the catalysts will therefore electrostatically attract dissociated cationic MB and repel dissociated anionic MO. A significant difference between pH_{PZC} of the catalyst and the pH of the dyes solutions implies a strong character of this effect. Therefore, the MB is expected to be adsorbed in a greater amount, which was confirmed by the laboratory results (Fig. 7).

As far as the surface properties, such as surface area, pore volume and average pore diameter are concerned (Table 2), it can be noticed that adsorption increases together with the increase of the surface area of the material (Fig. 7). The possibility of the contact of the catalyst with the solution during the photodegradation process also increases with its surface area. It can be clearly seen that the catalyst with the largest surface area (SiC-25—80.4 $m^2\ g^{-1}$) adsorbs in 60 min considerable amounts (even 17%) of MB from the solution. The content of TiO_2 in the TiO_2/beta-SiC catalysts influences also the average pore diameter, which varied in the range of 10.4–14.9 nm. Considering the longest spatial dimension of the dissociated form of the dyes, 1.43 and 1.49 for MB and MO, respectively, there is no preference for the particular dye in the adsorption. As the longest spatial dimension and the molecular weight of the MB and MO are similar (Table 3), in the process conditions, the pH of the reaction mixture and the catalysts surface area play the most important role.

Photodegradation of MB and MO

Because the photodegradation process was preceded by the adsorption step (section Adsorption of the organic pollutants), the C_0 has a different value for each experiment (Table 4). The percentage of MB and MO degradation over all the prepared photocatalysts is presented as a function of exposure time in Figs. 8 and 9, respectively. Both organic compounds used in our study are stable in the light source and process parameters (photolysis curves). It is also worth noting that the SiC-100 catalyst is almost not active at the applied process parameters. Using anatase as a catalyst (SiC-0) and composites containing TiO_2 and SiC (SiC-5–SiC-25, Table 1) significantly influences the photodegradation of MB and MO.

It can be clearly seen that in case of MB photodegradation, SiC presence in the TiO_2/SiC catalyst strongly affects the process effectiveness compared to the process with pure anatase (SiC-0) as catalyst. 5 wt. % of the SiC negatively influences photodegradation in the applied process parameters. Probably thick TiO_2 coating overshadows the light-sensitive SiC. That is why only TiO_2 phase is "active" in case of the SiC-5 catalyst, causing lowering the photodegradation level compared to the SiC-0 catalyst. With the β-SiC content at the level of 10–15 wt. %, photodegradation of methylene blue is highly efficient and what is also important, the dependence on the exposure time is close to linear—catalysts are stable and do not exhibit any signs of deactivation. The value of 15 wt. % of the β-SiC content in the catalyst (SiC-15) causes practically complete removal of the dye. This enhancement could be due to better conduction of electrons by the presence of SiC in TiO_2 and thus reduction in recombination of electron hole pair. This is due to relatively good dispersion of anatase on the SiC surface, and the materials heterojunction effect, described before by other authors (17,19,20). Significant decrease in catalyst activity was observed in case of the catalyst, in which SiC content was increased up to the value of 25 wt. % (Fig. 8), probably due to the large number of SiC particles insufficiently coated with TiO_2. At that point, 10–15 wt. % of β-SiC in the anatase/β-SiC catalyst can be pointed as the optimal. Probably, such behavior can be explained with the following reasons:

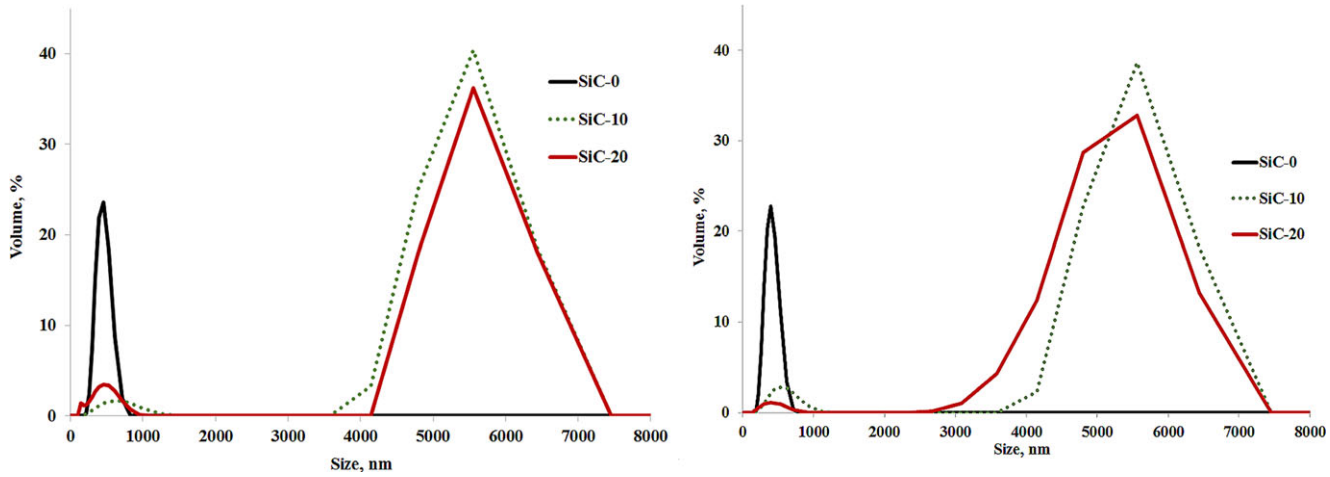

Figure 6. Catalysts particle size distribution measured with DLS method after the time of 5 min (A) and 15 min (B) sonication.

Table 3. Physicochemical properties of the applied dyes (42).

Characteristic	Methylene blue (MB)	Methyl orange (MO)
Molecular weight, g mol^{-1}	319.9	327.3
Topological polar surface area, $Å^2$	43.9	93.5
Solubility in water at 25°C, g dm^{-3}	43.6	5.0
The longest spatial dimension of the dissociated form of the molecule*, nm	1.43	1.49
pKa	3.80	3.47
100 ppm solution pH	7.21	6.55

*Calculated from DFT method—PBE0 functional/Def2-TZVP basis set.

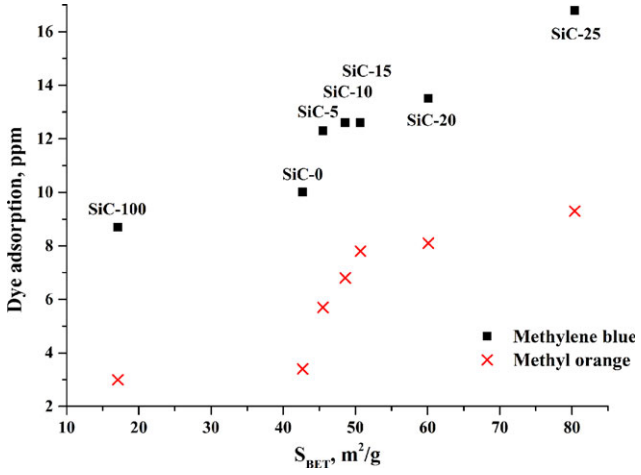

Figure 7. The correlation between BET catalysts surface area and the MB and MO adsorption level after 1 h of 100 ppm solution mixing with the catalyst concentration of 0.5 g L^{-1}. [Color figure can be viewed at wileyonlinelibrary.com]

1 a significant increase in the surface area of the SiC-10 and SiC-15 catalysts (comparing to the SiC-0) cause increase in the contact between catalyst surface and the MB,
2 preferable pH of the solution increase the contact catalyst-MB (dissociated molecule is attracted to the surface of the catalyst),
3 deagglomeration of TiO_2 on the surface of SiC in time probably favors the linear process flow.

Gómez-Solis *et al.* (20) studied photodegradation of methylene blue with the use of β-SiC–TiO_2 catalysts containing 20–80 wt.% of SiC. They have carried out the investigations on a solution with an initial concentration of 20 ppm and demonstrated that the most active catalyst is the one with the lowest share of SiC (20 wt. %). At the catalyst concentration of 1 g L^{-1}, apparent kinetic constant was noted at the level of 0.186 h^{-1} (20), which is very close to the apparent kinetic constant of SiC-20 obtained in the present study (0.180 h^{-1}—Table 5). This is regardless of two times lower catalyst concentration and five times higher MB concentration analyzed in this study. This confirms the assumption that TiO_2/beta-SiC catalysts are stable in assumed process conditions.

Although satisfactory results for the catalyst SiC-20 were obtained, SiC-15 proved to be the most effective catalyst with the apparent kinetic constant at the level of 0.238 h^{-1}. We suggest that the use of pH modifying agents, to increase the pH of MB solution, could accelerate the photodegradation process even more.

Table 4. Initial dye concentration in water solutions in photodegradation process at the applied TiO_2/β-SiC catalysts.

	C_0, ppm	
Catalyst	MB	MO
SiC-0	90.0	96.6
SiC-5	87.7	94.3
SiC-10	87.4	93.2
SiC-15	87.4	92.2
SiC-20	86.5	91.9
SiC-25	83.2	90.7
SiC-100	91.3	97.0

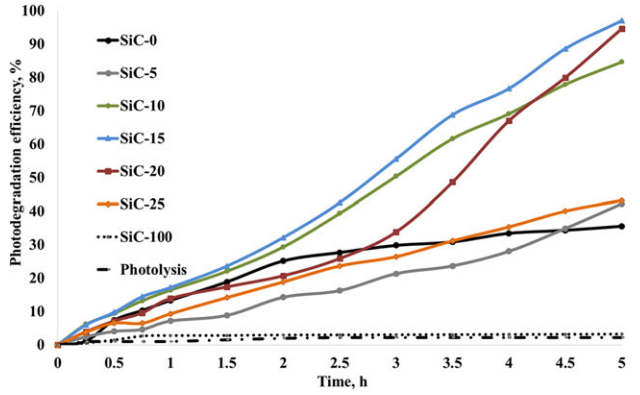

Figure 8. Photocatalytic efficiency of TiO_2/beta-SiC catalysts composition in methylene blue (MB) degradation under 100 W UV lamp radiation.

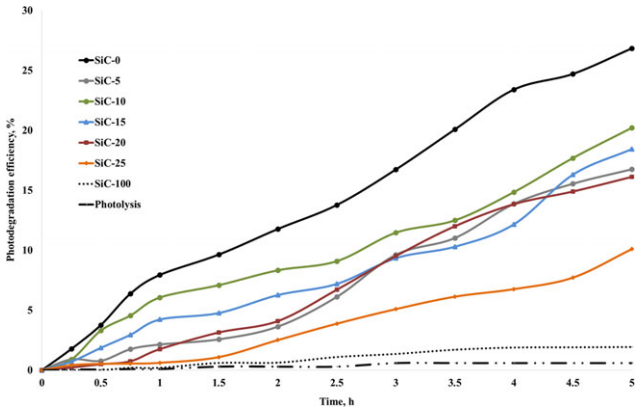

Figure 9. Photocatalytic efficiency of TiO_2/beta-SiC catalysts composition in methyl orange (MO) degradation under 100 W UV lamp radiation.

The efficiency of the MO photodegradation process (Fig. 9) is much lower than in the case of MB (Fig. 8). Maximum degradation of MO was observed at the level of 27% with SiC-0 catalyst. As the MB photodegradation process confirmed significant efficiency of the used photocatalysts, significant differences in efficiency of the MO photodegradation may be the result of the pH of the solution. Negatively charged surface of the catalysts repels the dissociated anionic MO molecules. A significant difference between catalysts pH_{PZC} and the pH of the dyes solutions (Tables 2 and 3) implies a strong character of this effect.

Table 5. Apparent kinetic constant and half-life time reaction for the TiO_2/beta-SiC catalysts in the experiment performed with 0.5 g L^{-1} catalyst concentration, 100 ppm initial dye concentration and 100 W UV lamp radiation.

	Methylene blue photodegradation			Methyl orange photodegradation		
Catalyst	k, h^{-1}	R^2	$t_{1/2}$, h	k, h^{-1}	R^2	$t_{1/2}$, h
SiC-0	0.040	>0.9	7.6	0.028	>0.9	10.8
SiC-5	0.056	>0.9	5.4	0.017	>0.9	18.0
SiC-10	0.150	>0.9	2.0	0.018	>0.9	17.1
SiC-15	0.238	>0.8	1.3	0.016	>0.9	18.5
SiC-20	0.180	>0.8	1.7	0.017	>0.9	17.9
SiC-25	0.059	>0.9	5.1	0.009	>0.9	33.8
SiC-100	0.003	–	115.8	0.002	>0.9	150.5

The closer the catalyst pH_{PZC} to the pH of the solution, the repulsion between the MO and the catalyst is weaker. Therefore, pure anatase (SiC-0) has the largest contact with the molecules of dye removed and was the most effective among all applied catalysts.

It has to be pointed out that pH_{PZC} is only one of the factors influencing the adsorption efficiency. While pH_{PZC} of the pure anatase and the SiC-25 catalyst do not differ much—5.85 *vs* 5.76, the surface area of the SiC-25 is almost twice higher—80.4 *vs* 42.7 m^2 g^{-1}. While this effect can be responsible for the increased adsorption, it does not explain low activity of the SiC-25. We conclude that in this case, the kinetics of the photodecomposition will be responsible for the overall efficiency.

The main effect of the pH_{PZC} *vs* solution pH will be observed for the MO *vs* MB adsorption, as both these molecules are present in the solution in the form of positively and negatively charged ions. This is indeed the case, MB adsorbs in all cases significantly better than MO.

Reaction kinetics

To study the reaction kinetics, the photocatalytic degradation of MB and MO as a function of time over the catalysts was investigated. The reaction rate was found to follow the Langmuir−Hinshelwood model as expressed by the equation $\ln(C_0/C) = kt$, where k is the apparent reaction rate constant and t is the reaction time. The value of k was determined from the slope photocatalytic degradation of MB and MO over all of the catalysts followed pseudo-first-order rates. The apparent rate constants, correlation coefficients (R^2) and half-times ($t_{1/2}$) of the photocatalytic degradation were evaluated and presented in Table 5. The apparent constants and half-times of dye photodegradation are consistent with the experimental results presented in Figs. 8 and 9. As mentioned before, the highest photocatalytic activity in case of MB photodegradation was observed with the use of SiC-15 as the catalyst. In case of MO, pH process conditions substantially minimize the contact of the catalyst with the dye that is why the process of photodegradation is reduced significantly —SiC-0 was the most active catalyst among all tested systems.

Mechanism

The insight into the mechanism of the process has been provided by molecular modeling. There are three possible mechanisms that

need to be taken into account—two direct ones, and one indirect with the attack of the active species formed by the water splitting at the catalyst surface. First direct mechanism is the photoactivation of the catalyst, and oxidation of the dye molecules by means of the electron transfer from the dye molecule to the hole generated in the VB of the catalyst. The second possibility is the direct photoactivation of the dye molecule and its reaction with the solvent or the catalyst surface. Both of these mechanisms can possibly proceed via the excited state of the dye molecule, either due to the direct photon absorption by the dye molecule or the excitation energy transfer from the catalyst via the Dixon mechanism (43). The latter would obviously strongly depend on the adsorption of the dye on the surface of the catalyst—the probability of the energy transfer is increased upon the contact of the molecules. This is consistent with the obtained results: The higher efficiency of the process correlates with significantly stronger adsorption for MB than for the MO molecule (Figs. 7–9).

The geometries of the dye molecules and their vertical excitation energies are gathered in Table 6. As both dyes are able to absorb the wavelength of the Hg lamp used (254 nm), they can also be directly photoexcited without the presence of the catalyst. This excitation, however, does not lead to the degradation of the dye molecules in the absence of the catalyst, as almost no photolysis has been observed experimentally (Figs. 8 and 9). Instead, in the absence of the catalyst, both molecules efficiently relax to the ground electronic state. The computational results are in agreement with this observation. The S_1 state of the MB molecule is the bright state (oscillator strength of 0.83), what means it is able to absorb the photon of UV light. The vibrational relaxation on the S_1 hypersurface is accompanied by the slight increase of the C-N bond length (from 1.32 to 1.42 Å) and leads to the minimum of the S_1 state with the energy of 1.50 eV with respect to the ground state energy. Interestingly, the T_1 state is more stable by approximately 0.1 eV, and therefore, the possibility of the crossing to the long-living triplet state can be assumed. The optimal geometry for the T_1 state is very similar to the S_1 state and does not show any significant distortions that could potentially lead to the bond dissociation. This is consistent with no activity observed for the photodegradation of the dye molecules in the absence of the catalyst.

The situation is different for the MO system, where the S_3 state is the electronically bright one; however, according to the Kasha's rule, the photorelaxation to the S_1 should be ultrafast (44). This state, however, is short-living one, due to the conical intersection that can be achieved barrierlessly and the MO molecule relaxes quickly to the ground state. The geometry of the system at the conical intersection represents the isomerization of azobenzene (14). However, with the lack of the dissociation of any bond in the dye molecule, it can be assumed that this factor is responsible for the photostability of the MO with no catalyst present.

Table 6. Vertical excitation energies of MO and MB molecules. Singlet and triplet states are denotes as S_x and T_x, respectively.

MB	MO
S_0 (ground state, reference) 0.0 eV	S_0 (ground state, reference) 0.0 eV
T_1 = 1.74 eV	T_1 = 2.33 eV
T_2 = 2.78 eV	T_2 = 2.65 eV
S_1 = 3.25 eV—oscillator strength 0.835	S_1 = 2.98 eV—oscillator strength 0.000
T_3 = 3.51 eV	T_3 = 3.13 eV
S_2 = 4.03 eV—oscillator strength 0.002	S_2 = 3.14 eV—oscillator strength 0.001
T_4 = 4.25 eV	S_3 = 3.49 ev—oscillator strength 1.002

Consequently, the mechanism of the photodegradation of the dye molecules appears to be indirect, occurring via the hydroxyl radicals generated at the surface of the catalyst as proposed in (2,3). This is also in agreement with very low degradation activity observed for pure 3C-SiC catalyst, which is much less active in the photocatalytic water splitting reaction, that is the source of the hydroxyl radicals in the solvent (45). However, in case of the nanocomposites, even small content of the SiC in the system increases the rate of the hydroxyl radical formation, which in turn oxidize the dye molecules. This holds for both MB and MO systems, with the difference of the facilitated recombination of the hydroxyl radical with the MB molecule, because of the diradical character of the long-living triplet state described above is much more reactive than the closed-shell ground state of the MO.

Furthermore, the proposed mechanism would strongly depend on the adsorption of the dyes on the catalyst surface. This influence is, however, not trivial to describe, and there are more effects that should be taken into account. The degradation of MB molecules is favored by several factors, for example the stability of long-lived excited state of the MB molecule and the enhanced adsorption on the catalyst surface. This, however, does not explain the decrease of the catalytic activity for the SiC-25 system, which has the most developed, best adsorbing surface. The results of Li *et al.* (45) suggest there is the optimum content of the SiC in the nanocomposite with TiO_2 corresponding with the maximum activity of the catalyst. This is the result of the charge transfer from SiC sites to TiO_2 due to the alignment of the VB. For the pure water splitting reaction, the optimal SiC content has been determined to be 5%, and the results obtained in this work show that the optimum for MB degradation is 15%. This discrepancy suggests that there still are other factors influencing the MB decomposition than the OH radical attack; however, the effect of decreasing the activity of TiO_2 by less active SiC seems to be present here as well.

The factors behind the degradation of the MO molecule are similar, and the reasons for lower activity are the weaker adsorption at the catalyst surface and fast relaxation from the excited to the ground state of the molecule. The main role seems to be played by the hydroxyl radicals generated at the catalyst surface. The maximum efficiency of the process is, however, observed for the pure TiO_2 catalyst, while the best adsorbing one is the one containing 25% of SiC and the maximum efficiency for the water splitting was determined to be for 5% of SiC (45).

CONCLUSIONS

TiO_2/β-SiC catalysts synthesized by the sol-gel method were found to be efficient catalysts for the methylene blue photodegradation under UV irradiation. At the optimal content of 15 wt. % of β-SiC and for the catalyst and dye concentrations of 0.5 g L^{-1} and 100 ppm, respectively, the apparent kinetic constant was noted at the level of 0.238 h^{-1}. Significantly lower activity was observed for methyl orange photodegradation at the same process parameters. In this case, maximum apparent kinetic constant was noted at the level of 0.028 h^{-1} with the use of pure anatase as the

photocatalyst. The pH of the solution plays the crucial role in the photodegradation of both investigated dyes, by means of supporting or limiting the contact of the catalyst with reactants.

The synergism between the two semiconductor materials was observed in case of the methylene blue photodegradation. The main reason for improving the photocatalytic properties of the materials could be the modification of the surface properties such as increasing the specific surface area and the pH_{PZC} variation. The energy band gap, which was observed at the level of 3.19–3.12 eV, was too small to influence the photodegradation process significantly. We conclude that the interaction between TiO_2 in the form of gel and a solid SiC does not occur at the significant level, and for the improvement of the heterojunction effect, a synthesis method other than sol-gel should be used.

Acknowledgements—This work was financed by statutory activity subsidy from the Polish Ministry of Science and Higher Education for the Faculty of Chemistry of Wroclaw University of Science and Technology. The authors would like to thank Jaśmina Szkawran, for the support in the photodegradation experiments. The computational results have been obtained thanks to the access to the BEM supercomputer at Wrocław Centre for Networking and Supercomputing (WCSS). The authors would like to thank Rafał Szabla for the support with the calculations and providing the access to the code for the conical intersection optimization. In addition, B.Sz. would like to thank R. Szabla for the priceless discussions on the topic of critical approach to one's own work.

REFERENCES

1. Linsebigler, A. L., G. Lu and J. T. Yates (1995) Photocatalysis on TiO_2 surfaces: principles, mechanisms, and selected results. *Chem. Rev.* **95**(3), 735–758.
2. Haque, M. M., D. Bahnemann and M. Muneer (2012) Photocatalytic Degradation of Organic Pollutants: Mechanisms and Kinetics. In *Organic Pollutants Ten Years After the Stockholm Convention - Environmental and Analytical Update* (Edited by T. Puzyn and A. Mostrag-Szlichtyng) InTech. Available from: http://www.intechopen.com/books/organic-pollutants-ten-years-after-the-stockholm-convention-environmental-and-analytical-update/photocatalytic-degradation-of-organic-pollutants-mechanisms-and-kinetics. Accessed 15 August 2016.
3. Zangeneh, H., A. A. L. Zinatizadeh, M. Habibi, M. Akia and M. I. Hasnain (2015) Photocatalytic oxidation of organic dyes and pollutants in wastewater using different modified titanium dioxides: a comparative review. *J. Ind. Eng. Chem.* **26**, 1–36.
4. Carp, O., C. L. Huisman and A. Reller (2004) Photoinduced reactivity of titanium dioxide. *Prog. Solid State Chem.* **32**, 33–177.
5. Dong, H., G. Zeng, L. Tang, C. Fan, C. Zhang, X. He and Y. He (2015) An overview of limitations of TiO_2-based particles for photocatalytic degradation of organic pollutants and the corresponding countermeasures. *Wat. Res.* **79**, 128–146.
6. Umar, M. and H. A. Aziz (2013) Photocatalytic degradation of organic pollutants in water. In *Organic Pollutants - Monitoring, Risk and Treatment* (Edited by M. N. Rashed), InTech. Available from: http://www.intechopen.com/books/organic-pollutants-monitoring-risk-and-treatment/photocatalytic-degradation-of-organic-pollutants-in-water. Accessed 15 August 2016.
7. Devi, L. G. and R. Kavitha (2013) A review on non-metal ion doped titania for the photocatalytic degradation of organic pollutants under UV/solar light: role of photogenerated charge carrier dynamics in enhancing the activity. *Appl. Catal. B Environ.* **140–141**, 559–587.
8. Pessoa, R. S., M. A. Fraga, L. V. Santos, M. Massi and H. S. Maciel (2015) Nanostructured thin films based on TiO_2 and/or SiC for use in photoelectrochemical cells: a review of the material characteristics, synthesis and recent applications. *Mater. Sci. Semicond. Process.* **29**, 56–68.
9. Fu, C. X., Y. Y. Gong, Y. T. Wu, J. Q. Liu, Z. Zhang, C. Li and L. Y. Niu (2016) Photocatalytic enhancement of TiO_2 by B and Zr co-doping and modulation of microstructure. *Appl. Surf. Sci.* **379**, 83–90.
10. Nabid, M. R., R. Sedghi, S. Gholami, H. A. Oskooie and M. M. Heravi (2013) Preparation of new magnetic nanocatalysts based on TiO2 and ZnO and their application in improved photocatalytic degradation of dye pollutant under visible light. *Photochem. Photobiol.* **89**, 24–32.
11. Sedghi, R. and F. Heidari (2016) A novel & effective visible light-driven TiO_2/magnetic porous graphene oxide nanocomposite for the degradation of dye pollutants. *RSC Adv.* **6**, 49459–49468.
12. Ghosh, S. and A. P. Das (2015) Modified titanium oxide (TiO_2) nanocomposites and its array of applications: a review. *Toxicol. Environ. Chem.* **97**(5), 491–514.
13. Szyja, B. M. and R. A. Van Santen (2015) Synergy between TiO_2 and Co_xO_y sites in electrocatalytic water decomposition. *Phys. Chem. Chem. Phys.* **17**, 12486–12491.
14. Ge, M., C. Guo, X. Zhu, L. Ma, Z. Han, W. Wu and Y. Wang (2009) Photocatalytic degradation of methyl orange using ZnO/TiO_2 composites. *Front. Environ. Sci. Engin. China* **3**(3), 271–280.
15. Li, S., Y.-H. Lin, B.-P. Zhang, J.-F. Li and C.-W. Nan (2009) $BiFeO_3$/TiO_2 core-shell structured nanocomposites as visible-active photocatalysts and their optical response mechanism. *J. Appl. Phys.* **105**(054310), 1–5.
16. Digdaya, I. A., L. Han, T. W. F. Buijs, M. Zeman, B. Dam, A. H. M. Smets and W. A. Smith (2015) Extracting large photovoltages from a-SiC photocathodes with an amorphous TiO_2 front surface field layer for solar hydrogen evolution. *Energ. Environ. Sci.* **8**, 1585–1593.
17. Lai, Y.-C. and Y.-C. Tsai (2012) An efficient 3C-silicon carbide/titania nanocomposite photoelectrode for dye-sensitized solar cell. *Chem. Commun.* **48**, 6696–6698.
18. Hao, D., Z. Yang, C. Jiang and J. Zhang (2014) Synergistic photocatalytic effect of TiO_2 coatings and p-type semiconductive SiC foam supports for degradation of organic contaminant. *Appl. Catal. B Environ.* **144**, 196–202.
19. Mishra, G., K. M. Parida and S. K. Singh (2014) Solar light driven Rhodamine B degradation over highly active β-SiC-TiO_2 nanocomposite. *RSC Adv.* **4**, 12918–12928.
20. Gómez-Solis, C., I. Juarez-Ramirez, E. Moctezuma and L. M. Torres-Martinez (2012) Photodegradation of indigo carmine and methylene blue dyes in aqueous solution by SiC-TiO_2 catalysts prepared by sol-gel. *J. Hazard. Mater.* **217–218**, 194–199.
21. Chem, Z., F. Bing, Q. Liu, Z. Zhang and X. Fang (2015) Novel Z-scheme visible-light-driven Ag_3PO_4/Ag/SiC photocatalysts with enhanced photocatalytic activity. *J. Mater. Chem. A* **3**, 4652–4658.
22. Turchi, C. S. and D. F. Ollis (1990) Photocatalytic degradation of organic-water contaminants- mechanisms involving hydroxyl radical attack. *J. Catal.* **122**, 178–192.
23. Parra, S., J. Olivero and L. C. Pulgarin (2002) Relationships between physicochemical properties and photoreactivity of four biorecalcitrant phenylurea herbicides in aqueous TiO_2 suspension. *Appl. Catal. B Environ.* **36**, 75–85.
24. Doong, R.-A., C.-H. Chen, R. A. Maithreepala and S.-M. Chang (2001) The influence of pH and cadmium sulfide on the photocatalytic degradation of 2-chlorophenol in titanium dioxide suspensions. *Wat. Res.* **35**, 2873–2880.
25. Schmelling, D. C., K. A. Gray and P. V. Kamat (1997) The influence of solution matrix on the photocatalytic degradation of TNT in TiO_2 slurries. *Wat. Res.* **31**, 1439–1447.
26. Sarma, B. K., A. R. Pal, H. Bailung and J. Chutia (2013) Growth of nanocrystalline TiO_2 thin films and crystal anisotropy of anatase phase deposited by direct current reactive magnetron sputtering. *Mater. Chem. Phys.* **139**, 979–987.
27. Akhter, P., M. Hussain, G. Saracco and N. Russo (2015) Novel nanostructured-TiO_2 materials for the photocatalytic reduction of CO_2 greenhouse gas to hydrocarbons and syngas. *Fuel* **149**, 55–65.
28. López, R. and R. Gómez (2012) Band-gap energy estimation from diffuse reflectance measurements on sol-gel and commercial TiO2: a comparative study. *J. Sol-Gel. Sci. Technol.* **61**, 1–7.
29. Murphy, A. B. (2007) Band-gap determination from diffuse reflectance measurements of semiconductor films, and application of

photoelectrochemical water-splitting. *Sol. Energy Mater. Sol. Cells* **91**, 1326–1337.
30. Moreno-Castilla, C., M. V. Lopez-Ramon and F. Carrasco-Marin (2000) Changes in surface chemistry of activated carbons by wet oxidation. *Carbon* **38**, 1995–2001.
31. TURBOMOLE V6.6 2014, a development of University of Karlsruhe and Forschungszentrum Karlsruhe GmbH, 1989–2007, TURBOMOLE GmbH, since 2007; http://www.turbomole.com. Accessed on 15 June 2016.
32. Adamo, C. and V. Barone (1999) Toward reliable density functional methods without adjustable parameters: the PBE0 model. *J. Chem. Phys.* **110**, 6158–6170.
33. Weigend, F. and R. Ahlrichs (2005) Balanced basis sets of split valence, triple zeta valence and quadruple zeta valence quality for H to Rn: design and assessment of accuracy. *Phys. Chem. Chem. Phys.* **7**, 3297–3305.
34. Weigend, F. (2006) Accurate Coulomb-fitting basis sets for H to Rn. *Phys. Chem. Chem. Phys.* **8**, 1057–1065.
35. Häaettig, C. and K. Hald (2002) Implementation of RI-CC2 triplet excitation energies with an application to trans-azobenzene. *Phys. Chem. Chem. Phys.* **4**, 2111–2118.
36. Dunning, T. H. Jr (1989) Gaussian basis sets for use in correlated molecular calculations. I. The atoms boron through neon and hydrogen. *J. Chem. Phys.* **90**, 1007–1023.
37. Kendall, R. A., T. H. Jr Dunning and R. J. Harrison (1992) Electron affinities of the first-row atoms revisited. Systematic basis sets and wave functions. *J. Chem. Phys.* **96**, 6796–6806.
38. Woon, D. E. and T. H. Jr Dunning (1993) Gaussian-basis sets for use in correlated molecular calculations. 3. The atoms aluminum through argon. *J. Chem. Phys.* **98**, 1358–1371.
39. Szabla, R., R. W. Góra and J. Šponer (2016) Ultrafast excited-state dynamics of isocytosine. *Phys. Chem. Chem. Phys.* **18**, 20208–20218.
40. Warren, B. E. (1969) *X-Ray Diffraction*. Addison-Wesley Publishing Company Inc, New York, NY.
41. Colmenares, J. C., R. Luque, J. M. Campelo, F. Colmenares, Z. Karpiński and A. Romero (2009) Nanostructured photocatalysts and their applications in the photocatalytic transformation of lignocellulosic biomass: an overview. *Materials* **2**, 2228–2258.
42. http://pubchem.ncbi.nlm.nih.gov. Accessed on 10 August 2015.
43. Förster Th (1960) Transfer Mechanisms of Electronic Excitation Energy, Proceedings of a Symposium Sponsored by the U. S. Atomic Energy Commission Held at Brookhaven National Laboratory, October 12–16, 1959, pp. 326–339.
44. IUPAC (1997) *Compendium of Chemical Terminology*, 2nd ed. (the "Gold Book"). Compiled by A. D. McNaught and A. Wilkinson. Blackwell Scientific Publications, Oxford. XML on-line corrected version: http://goldbook.iupac.org (2006) created by M. Nic, J. Jirat, B. Kosata; updates compiled by A. Jenkins. ISBN 0-9678550-9-8. doi: 10.1351/goldbook.
45. Li, Y., Z. Yu, J. Meng and Y. Li (2013) Enhancing the activity of a SiC-TiO_2 composite catalyst for photo-stimulated catalytic water splitting. *Int. J. Hydrogen Energy* **38**, 3898–3904.